International Journal of Solids and Structures 49 (2012) 3397–3408

Contents lists available at SciVerse ScienceDirect

International Journal of Solids and Structures

journal homepage: www.elsevier.com/locate/ijsolstr

Computationally generated cross-property bounds for stiffness and fluid permeability using topology optimization

Vivien J. Challis [a,*], James K. Guest [b], Joseph F. Grotowski [a], Anthony P. Roberts [a]

[a] School of Mathematics and Physics, The University of Queensland, St Lucia, Brisbane, QLD 4072, Australia
[b] Department of Civil Engineering, Johns Hopkins University, 3400 N. Charles Street, Baltimore, MD 21218, United States

ARTICLE INFO

Article history:
Received 13 March 2012
Received in revised form 18 June 2012
Available online 3 August 2012

Keywords:
Topology optimization
Multifunctional materials
Pareto fronts
Cross-property bounds
Fluid permeability
Bulk modulus

ABSTRACT

We compute Pareto fronts that estimate the upper bounds of the bulk modulus and fluid permeability cross-property space for periodic porous materials over a range of porosities. The fronts are generated numerically using topology optimization, which is a systematic, free-form design algorithm for optimizing material layouts. The presented microstructures demonstrate the trade-off between the bulk modulus and fluid permeability achievable with a multifunctional porous material and will be useful for designers of materials for which both stiffness and permeability are important. Our results suggest that the range of achievable stiffness and permeability properties is significantly restricted when considering elastic isotropy, as compared to cubic elastic symmetry. The estimated bounds are of practical importance given the lack of microstructure-independent theoretical cross-property bounds.

1. Introduction

The range of possible effective properties of heterogeneous materials composed of distinct material phases is not only of interest from a scientific viewpoint, but also in the design of engineered materials. Such ranges are needed for optimizing material selection and assessing material design quality. Hashin and Shtrikman (1962) pioneered this field by deriving the now well-known Hashin–Shtrikman bounds on the effective magnetic permeability of composites. By mathematical analogy, their result also applies to the electrical conductivity, thermal conductivity, dielectric constant and diffusion coefficient. Hashin and Shtrikman (1963) also bounded the effective elastic bulk and shear moduli of two-phase composites consisting of elastically isotropic phases for the case that the phase with the larger shear modulus also has the larger bulk modulus, or so-called well-ordered phases. Walpole (1966) generalized these bounds, removing the restriction on the relative properties of the two phases.

The determination of rigorous bounds on a single effective property led to another fundamental question: can two different properties of a heterogeneous material be rigorously linked to one another to determine the range of possible effective properties in the multidimensional property space? Such cross-property bounds have important implications for the design of multifunctional composites and are furthermore useful from a practical viewpoint, particularly in the case that one physical property is easier to measure than another (Torquato, 2002). It is intuitive that cross-property relations might exist, because knowing the value of one effective property provides some microstructural information that should allow another effective property to be bounded. Explicit cross-property connections that are independent of microgeometry can be established when the microstructural parameters controlling the two effective properties are sufficiently similar (Sevostianov and Kachanov, 2009).

A number of cross-property relations have been derived in the literature. For example: established cross-property bounds link the effective thermal conductivity and the effective electrical conductivity of isotropic two-phase media (Bergman, 1978; Avellaneda et al., 1988); and bounds linking the effective bulk modulus and effective shear modulus in isotropic two-phase composites with isotropic phases (Berryman and Milton, 1988; Cherkaev and Gibiansky, 1993) improve upon the earlier Hashin and Shtrikman (1963) bounds.

Cross-property bounds relating effective properties determined by different governing equations have also been considered, and much of this work has been related to the elasticity and conductivity problem. The tightest such cross-property bounds were presented by Gibiansky and Torquato (1993, 1995, 1996). The distribution of the material phases has a similar effect on the effective elastic and conductive properties of a composite, leading to cross-property bounds that are independent of microgeometry: See discussion in Sevostianov and Kachanov (2009). That is, the elasticity and conductivity cross-property bounds only depend on the volume fractions and bulk physical properties of the material phases.

* Corresponding author. Tel.: +61 7 33652302; fax: +61 7 33651477.
E-mail address: vchallis@maths.uq.edu.au (V.J. Challis).

0020-7683/$ - see front matter © 2012 Elsevier Ltd. All rights reserved.
http://dx.doi.org/10.1016/j.ijsolstr.2012.07.019

In this work, the properties of interest are the bulk modulus and fluid permeability of porous materials. Avellaneda and Torquato (1991) derived cross-property bounds that link the fluid permeability and conductivity of a porous material under the assumptions that the solid material is insulating and the physical properties relate to the porous space filled with electrolyte. These bounds can be combined with conductivity and elasticity cross-property bounds (described above) to determine relationships between the permeability and the elastic properties of a porous material. However, these relations are microstructure dependent (Torquato, 2002; cf. Sevostianov and Kachanov, 2009): the effective length parameter in the relation between the permeability and the conductivity is dependent on the microgeometry. Furthermore, its calculation is as difficult as the calculation of the permeability itself (Torquato, 2002, p. 652).

In the absence of microstructure-independent cross-property bounds for the stiffness and fluid permeability of porous materials, we turn to topology optimization to search for structures with properties along the upper bound of the effective bulk modulus and fluid permeability cross-property space. Topology optimization is a systematic numerical approach that optimizes the layout of a material within a specified domain, including the determination of both the topology and the geometry of the material layout. The topology optimization of material microstructures was pioneered by Sigmund (1994) to design truss-like material structures with negative Poisson's ratio, and then extended to a more general method for continuum elasticity (e.g., Sigmund and Torquato, 1997; Gibiansky and Sigmund, 2000). In this approach, the material microstructure to be optimized is assumed to be periodic, and its smallest repetitive unit is referred to as the base cell. The effective (or macroscopic) properties of the material can be determined by homogenization via an analysis of the physical response of the base cell. The problem of finding materials with desired effective properties is called inverse homogenization and can be effectively solved using topology optimization. Bendsøe and Sigmund (2004) provide an overview of this approach.

Previous studies have demonstrated the capability of topology optimization for finding material microstructures that achieve theoretical bounds. Topology optimization was used by Sigmund (2000) with solid-void microstructures and Gibiansky and Sigmund (2000) with 3-phase microstructures to obtain results with effective bulk moduli within a few percent of the theoretical bound. In the case of cross-property bounds, Torquato et al. (2002, 2003) optimized structures for the simultaneous transport of heat and electricity and obtained a structure with a phase interface resembling a Schwartz primitive minimal surface. They further determined that microstructures with the Schwartz primitive or diamond surfaces as the phase interface numerically attained effective transport properties on the cross-property bound. The capability of topology optimization for achieving cross-property bounds has also been shown for properties with different governing equations: Challis et al. (2008) presented optimized isotropic microstructures with effective properties very close to the bulk modulus and conductivity cross-property bounds for a range of volume fractions of the stiff and conductive phases.

The use of topology optimization can also lead to new understanding of theoretical bounds and their attainability. In the case of thermoelastic properties, the discrepancy between the properties of topology optimized materials presented in Sigmund and Torquato (1997) and the prevailing theoretical bounds (Schapery, 1968; Rosen and Hashin, 1970) motivated a significant tightening of the theoretical bounds by Gibiansky and Torquato (1997). Topology optimization results have also inspired the discovery of new classes of composites with elastic properties attaining the relevant bounds (Sigmund, 2000; Gibiansky and Sigmund, 2000).

We utilize topology optimization to estimate the extent of the stiffness and fluid permeability cross-property space for porous materials. This problem is not just important from a scientific viewpoint — stiffness and fluid permeability are both relevant for the design of filters, actuators (Andreasen and Sigmund, 2011), and porous bone implant scaffolds for medical applications (Hollister, 2005, 2009; Chen et al., 2009, 2011; Challis et al., 2010). Guest and Prévost (2006a) considered a special case of this problem, namely that of a solid volume fraction of 50%, cubic elastic symmetry and isotropic flow symmetry. Here we also consider isotropic flow symmetry, but consider a range of solid volume fractions and both cubic and isotropic elastic symmetry. We find Pareto fronts of optimized solutions for this multi-objective optimization problem that estimate the upper bound of the bulk modulus and fluid permeability cross-property space. Our computationally-derived cross-property bounds include many new optimized microstructures, reveal a dependency on elastic symmetry not seen in stiffness-conductivity bounds, and should prove useful in applications, particularly given the lack of microstructure-independent theoretical cross-property bounds.

The remainder of this paper is as follows. We describe the design problem in detail in Section 2. In Section 3 we describe our optimization methods, and our results are presented in Section 4. In Section 5 we discuss our results, and our concluding remarks are given in Section 6.

2. Inverse homogenization formulation

We consider periodic porous materials characterized by a representative base unit cube. The two phases in the base cell are a solid material of Young's modulus $E = 1$ and Poisson's ratio $\nu = 0.3$, and a void phase through which fluid may flow. The base cell is represented with hexahedral finite elements (i.e., cubes). Our goal is to identify each element as being either solid or void, corresponding to the specification of $\rho_e = 1$ or $\rho_e = 0$, respectively, for each element e.

In the following subsections we outline the homogenization process and relevant symmetry requirements of the effective elastic and flow properties. We then formulate our topology optimization problem.

2.1. Elastic homogenization

The goal of the elastic homogenization process is to determine the effective elasticity tensor $\mathbf{C}^H$ that relates the macroscopic stress tensor $\boldsymbol{\sigma}$ to the macroscopic strain tensor $\boldsymbol{\epsilon}$ for the porous material via the linear elasticity law

$$\boldsymbol{\sigma} = \mathbf{C}^H \boldsymbol{\epsilon}, \tag{1}$$

where for convenience we have utilized the standard matrix representation of the rank 4 elasticity tensor and the associated vector representation for the stress and strain tensors. The superscript H is used here to denote a homogenized property. Finding the components of $\mathbf{C}^H$ requires solving the equations of linear elasticity for six independent strain fields applied to the unit cell with periodic boundary conditions. These local strain and stress fields are then averaged over the base cell to find the components of the elasticity tensor (Bensoussan et al., 1978; Sanchez-Palencia, 1980). Our finite element approach for this homogenization process is entirely standard. Equations and detailed references for this process can be found, for example, in Guedes and Kikuchi (1990), Hassani and Hinton (1998), and Garboczi and Day (1995).

We seek to explore the stiffness and fluid permeability cross-property space for each of cubic and isotropic elastic symmetry.

A material with cubic elastic symmetry has an effective stiffness matrix with three independent components of the form

$$\boldsymbol{C}^H = \begin{bmatrix} C_{11}^H & C_{12}^H & C_{12}^H & 0 & 0 & 0 \\ C_{12}^H & C_{11}^H & C_{12}^H & 0 & 0 & 0 \\ C_{12}^H & C_{12}^H & C_{11}^H & 0 & 0 & 0 \\ 0 & 0 & 0 & C_{44}^H & 0 & 0 \\ 0 & 0 & 0 & 0 & C_{44}^H & 0 \\ 0 & 0 & 0 & 0 & 0 & C_{44}^H \end{bmatrix}. \tag{2}$$

A material with isotropic elastic symmetry has one further relation between its components, meaning that only two independent components remain to give an effective stiffness matrix of the form

$$\boldsymbol{C}^H = \begin{bmatrix} C_{11}^H & C_{12}^H & C_{12}^H & 0 & 0 & 0 \\ C_{12}^H & C_{11}^H & C_{12}^H & 0 & 0 & 0 \\ C_{12}^H & C_{12}^H & C_{11}^H & 0 & 0 & 0 \\ 0 & 0 & 0 & \frac{1}{2}(C_{11}^H - C_{12}^H) & 0 & 0 \\ 0 & 0 & 0 & 0 & \frac{1}{2}(C_{11}^H - C_{12}^H) & 0 \\ 0 & 0 & 0 & 0 & 0 & \frac{1}{2}(C_{11}^H - C_{12}^H) \end{bmatrix}. \tag{3}$$

The bulk modulus B^H measures a material's resistance to volumetric strain, and is a stiffness measure that is often optimized in the topology optimization literature (Bendsøe and Sigmund, 2004). For cubic or isotropic materials, the effective bulk modulus B^H for the material is related to the components of $\boldsymbol{C}^H$ via

$$B^H = \frac{1}{3}C_{11}^H + \frac{2}{3}C_{12}^H. \tag{4}$$

2.2. Stokes flow homogenization

The homogenization of Stokes flows through a porous material gives Darcy's law on the macroscopic scale, which states that

$$\boldsymbol{U} = -\frac{1}{\mu}\boldsymbol{K}^H \nabla P, \tag{5}$$

where $\boldsymbol{U}$ is the average fluid velocity, ∇P is the pressure gradient across the material, $\boldsymbol{K}^H$ is the effective fluid permeability tensor and μ is the viscosity of the fluid. Calculation of the fluid permeability tensor requires the solution of a set of scaled Stokes flow equations (see Appendix A). This corresponds to solving Stokes equations for three independent unit body forces applied to the unit cell. Our numerical approach to the fluid homogenization follows the method described by Guest and Prévost (2006a, 2007).

The effective permeability tensor $\boldsymbol{K}^H$ for a general material is symmetric and therefore has six independent components. A material with isotropic flow symmetry has an effective permeability tensor that is isotropic, meaning that it is of the form

$$\boldsymbol{K}^H = k^H \boldsymbol{I}, \tag{6}$$

where k^H is the effective scalar fluid permeability and $\boldsymbol{I}$ is the identity tensor.

2.3. Multi-objective optimization problem and solution strategy

Searching for the upper-bound of the bulk modulus and fluid permeability cross-property space requires solving the multi-objective optimization problem

$$\begin{aligned} \max_{\boldsymbol{\rho}} \quad & [B^H(\boldsymbol{\rho}), k^H(\boldsymbol{\rho})] \\ \text{subject to} \quad & \phi(\boldsymbol{\rho}) = \phi^* \\ & \boldsymbol{g}(\boldsymbol{C}^H(\boldsymbol{\rho}), \boldsymbol{K}^H(\rho)) \leqslant \boldsymbol{0} \\ & \boldsymbol{h}(\boldsymbol{\rho}) = \boldsymbol{0}. \end{aligned} \tag{7}$$

Here $\boldsymbol{\rho}$ is the vector of design variables $\rho_e \in \{0,1\}$ for each element e, ϕ^* is the required porosity of the porous material, and $\phi(\boldsymbol{\rho})$ is the porosity of the material calculated as the proportion of elements e with $\rho_e = 0$. In practice the porosity constraint is implemented with a tolerance of 1%. The equality constraint $\boldsymbol{h}(\boldsymbol{\rho}) = \boldsymbol{0}$ represents the homogenization and associated equilibrium equations. The inequalities $\boldsymbol{g}(\boldsymbol{C}^H(\boldsymbol{\rho}), \boldsymbol{K}^H(\rho)) \leqslant \boldsymbol{0}$ represent the constraints on the effective constitutive tensors, including symmetry constraints. We will consider two cases of symmetry constraints: (1) cubic symmetry for the elastic properties with isotropic flow symmetry; and (2) isotropic symmetry for the elastic properties with isotropic flow symmetry.

For multi-objective optimization problems there is not typically a single optimal solution: in general, a solution that maximizes one objective will not maximize the other objectives (Cohon, 1978). This is certainly the case for the bulk modulus and fluid permeability problem, because maximal bulk modulus materials are closed-cell materials with disconnected pore spaces (Sigmund, 1999) that therefore have zero fluid permeability. What we are instead searching for is the set of noninferior solutions. These are feasible solutions to the optimization problem for which no other feasible solution exists that has a larger value for both of the objectives (Cohon, 1978). The notion of noninferior solutions is the same as Pareto optimality, a term first used by economists and used in the topology optimization literature (e.g., Chen et al., 2010; de Kruijf et al., 2007). The set of noninferior (or Pareto-optimal) solutions forms the Pareto front. It is this front that will provide our estimate for the upper-bound of the bulk modulus and fluid permeability cross-property space. See the explanatory diagram in Fig. 1(a).

To find structures on the Pareto front for the multi-objective optimization problem in Eq. (7), a common approach is to weight the two objectives and solve the optimization problem

$$\begin{aligned} \max_{\boldsymbol{\rho}} \quad & f(B^H(\boldsymbol{\rho}), k^H(\boldsymbol{\rho})) = \omega_B \frac{B^H(\boldsymbol{\rho})}{B^*} + \omega_k \frac{k^H(\boldsymbol{\rho})}{k^*} \\ \text{subject to} \quad & \phi(\boldsymbol{\rho}) = \phi^* \\ & \boldsymbol{g}(\boldsymbol{C}^H(\boldsymbol{\rho}), \boldsymbol{K}^H(\rho)) \leqslant \boldsymbol{0} \\ & \boldsymbol{h}(\boldsymbol{\rho}) = \boldsymbol{0}. \end{aligned} \tag{8}$$

Here ω_B and ω_k are weights satisfying $\omega_B + \omega_k = 1$ and dictating the relative importance of bulk modulus and fluid permeability in this single-objective optimization problem. The two terms in this objective are normalized appropriately: B^* and k^* are the maximum bulk modulus and fluid permeability subject to the same constraints, found by solving the optimization problem with $\omega_B = 1$, $B^* = 1$, $\omega_k = 0$ and $\omega_B = 0$, $\omega_k = 1$, $k^* = 1$. respectively. The solutions of these two optimization problems give structures at the endpoints of the Pareto front.

It is known that the success of the linear combination approach in finding the Pareto front depends on the convexity of the solution space (Kim and de Weck, 2005). As explained in Fig. 1(b) and (c), if the solution space is convex then this linear combination strategy will allow us to fully explore the front. This is the case for the stiffness-conductivity problem (e.g., Chen et al., 2010; de Kruijf et al., 2007). However, in the case of stiffness and permeability, we have found that the solution space is not convex and portions of the Pareto fronts cannot be found by optimizing Eq. (8) for a range of weights. Our strategy for finding structures on the Pareto front in this case is to maximize permeability subject to a constraint on the minimum bulk modulus. Thus in Eq. (8), $\omega_B = 0$ and the set

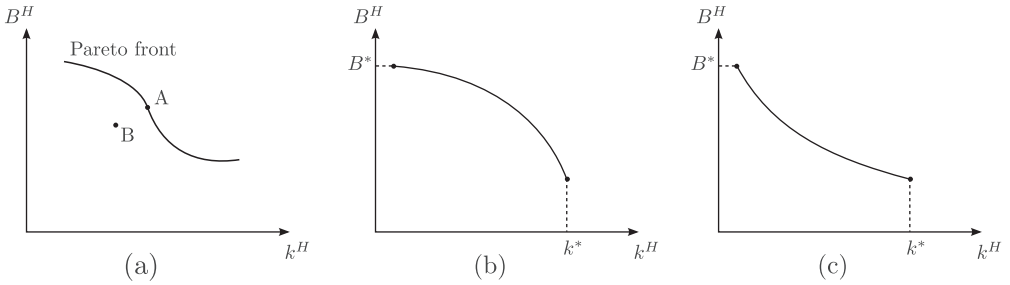

Fig. 1. (a) An illustration of the meaning of noninferior or Pareto-optimal feasible solutions for the bulk modulus and permeability problem. Point A corresponds to a noninferior solution that lies on the Pareto front. Point B corresponds to an inferior solution because the solution corresponding to point A has larger bulk modulus and permeability than at B. (b, c) Illustrations of the Pareto front between the maximum bulk modulus solution (with bulk modulus B^*) and the maximum permeability solution (with permeability k^*). In (b), the cross-property space is a convex set and solutions along the front can be found by maximizing a linear combination of the bulk modulus and fluid permeability as in Eq. (8). In (c), the cross-property space is not a convex set and solutions on the Pareto front between the maximum bulk modulus and maximum permeability solutions cannot be found by maximizing a linear combination of the bulk modulus and permeability. (All diagrams are assumed to correspond to specified porosity and symmetry constraints.)

of inequalities $\boldsymbol{g}$ includes $B^H(\boldsymbol{\rho}) \geqslant B^H_{min}$. This constraint-based approach is standard (e.g., Cohon, 1978).

3. Topology optimization algorithms

We utilize the level set method of topology optimization (Wang et al., 2003; Allaire et al., 2004) and follow the methods developed by Challis et al. (2008) for optimizing three-dimensional microstructures with the level set method, including their algorithm for imposing symmetry constraints. The reader is therefore referred to the earlier work of Challis et al. (2008) for the main details of the level set algorithm.

Level set methods are well suited for topology optimization problems involving fluid flow (Kreissl et al., 2011; Challis and Guest, 2009). In particular, Challis and Guest (2009) demonstrated that a level set method that maintains discrete element densities $\rho_e \in \{0,1\}$ can efficiently optimize Stokes flows. Maintaining discreteness allows a direct and exact implementation of the no-slip boundary condition at the solid–fluid interface. The flow equations therefore do not need to be solved in the solid regions, leading to enhanced computational efficiency compared with material distribution topology optimization approaches (Borrvall and Petersson, 2003; Guest and Prévost, 2006b). The calculation of the shape derivative of the homogenized fluid permeability tensor is outlined in Appendix A and this result is needed for optimizing the fluid permeability with the level set algorithm.

The initial condition for the presented optimization results is a three-dimensional cross structure (Challis et al., 2008) with porosity $\phi = 0.5$. Other initial structures were also considered, but these resulted in optimized structures with inferior properties (see Section 5.3). The cross structure is a good choice because it has simple cubic symmetry and each phase is connected across the base cell. In addition, the solid and void phases of the structure are equivalent, preventing bias toward the elastic properties over the fluid permeability, or vice versa. Given the cubic symmetry of this starting material, it has cubic elastic symmetry and isotropic flow symmetry. These characteristics were observed to be maintained in our algorithm throughout the optimization process: at no stage does the structure being optimized lose this cubic symmetry and associated symmetry of the elastic and flow properties.

When optimizing with the requirement of isotropic elastic symmetry, the anisotropy of the elastic properties of the material microstructure is denoted by $\mathcal{A}$ and calculated as in Challis et al. (2008). This anisotropy value is essentially a measure of the "distance" between the elasticity tensor of the microstructure and that of the isotropic material with the "closest" elasticity tensor, normalized by the magnitude of the properties of the material. The cubic symmetry of the starting structure is still retained when optimizing with the requirement of isotropic elastic symmetry. Given this cubic symmetry, the anisotropy measure $\mathcal{A}$ can be calculated for our structures simply with the formula

$$\mathcal{A} = \frac{12(C^H_{11} - C^H_{12} - 2C^H_{44})^2}{25(C^H_{11} + 2C^H_{12})^2 + 5(2C^H_{11} - 2C^H_{12} + 6C^H_{44})^2}. \tag{9}$$

Here $\mathcal{A}$ and the stiffness matrix components depend on the design variables $\boldsymbol{\rho}$. For an isotropic structure the relation $C^H_{44} = \frac{1}{2}(C^H_{11} - C^H_{12})$ is satisfied, and in this case the numerator of the anisotropy measure correctly gives zero. The elastic isotropy constraint is implemented as $\mathcal{A}(\rho) \leqslant 0.01$ (this is the choice of $\boldsymbol{g}(\boldsymbol{\rho})$ in Eq. (7)), and all of the microstructures presented here that were optimized with the requirement of elastic isotropy either satisfy this condition, or they have a disconnected solid phase and are therefore trivially isotropic.

A new aspect of our algorithm is the capability of constraining the bulk modulus to a particular value while maximizing the fluid permeability. This is approached heuristically: when the bulk modulus is below the required value, the bulk modulus is given a high priority in the objective function for that iteration of the optimization; and when the bulk modulus is above its required value the permeability is given precedence instead. This process continues until convergence, at which point the competing requirements of matching the specified bulk modulus and maximizing the fluid permeability have reached the correct balance. Despite its heuristic nature the algorithm works well.

As is typical of topology optimization methods, our algorithm involves many parameters that may have an impact on the solution determined by the optimization process. To ensure that we obtained the best optimized microstructures we solved each optimization problem with a range of parameters and the noninferior solutions were retained for generating the Pareto fronts.

4. Optimization results

Computationally-derived Pareto fronts and the corresponding optimized base cells with $40 \times 40 \times 40$ elements are presented in Figs. 2–4 for the three porosities $\phi = 0.5$, $\phi = 0.75$ and $\phi = 0.25$, respectively. We also present the maximum stiffness and maximum permeability optimized designs for porosities $\phi = 0.9$ and $\phi = 0.1$ in Figs. 5 and 6, respectively. For each optimized material microstructure the left structure (pink online) shows the solid phase of the base cube and the right structure (blue online) shows the void phase of the base cube through which fluid can flow. For clarity, the center of the base cell has been shifted by half the base

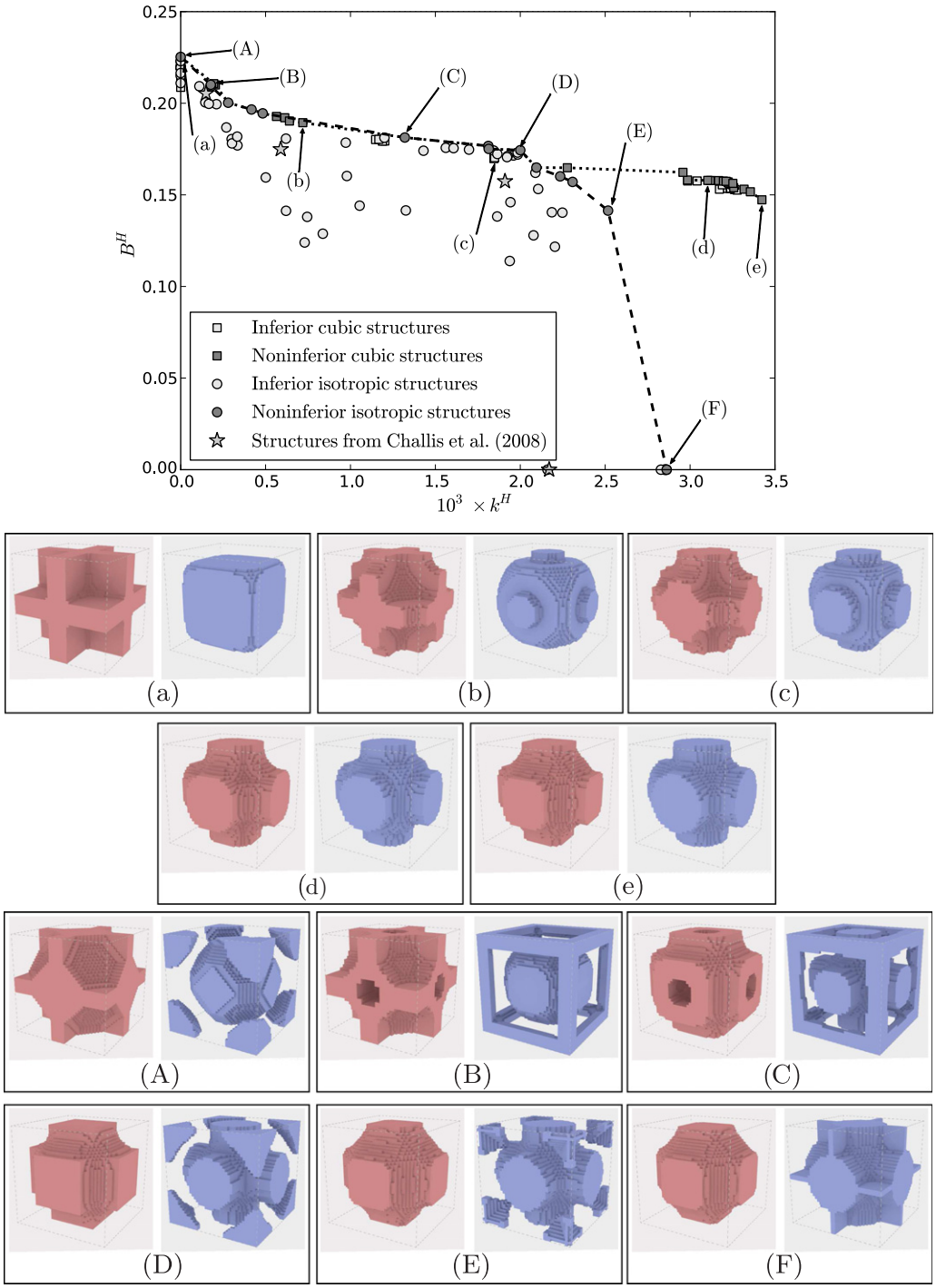

Fig. 2. Optimization results for porosity $\phi = 0.5$ with isotropic flow symmetry and either cubic (lowercase letters, square markers) or isotropic (uppercase letters, circular markers) elastic symmetry. The noninferior optimization results are shown with darker markers and are joined with lines (dotted for cubic elastic symmetry, dashed for isotropic elastic symmetry) that estimate the Pareto fronts. The properties of structures with $\phi = 0.5$ optimized for bulk modulus and conductivity by Challis et al. (2008) are indicated by the star markers (see discussion in Section 5.2). For the base cells presented in (a)–(F), the left structure (pink online) shows the solid phase and the right structure (blue online) shows the void phase translated by half of the base cell edge length along each coordinate direction.

cell edge length along each dimension for the depiction of the void phase.

The properties of the presented optimized microstructures are provided in Tables 1–5. All permeability values are scaled by the face area of the base cell and the bulk modulus values are computed with a Young's modulus of 1 and a Poisson's ratio of 0.3 for the solid phase. Structures for which the fluid phase of the design is disconnected are listed with a permeability of zero. The computational calculations of the fluid permeability would give a value of the order of 10^{-5}. The anisotropy measure $\mathcal{A}$ for structures with a disconnected solid phase is also given as zero.

5. Discussion

To aid in our discussion, Fig. 7 shows the results for porosities $\phi = 0.25$, $\phi = 0.5$ and $\phi = 0.75$ together on the same axes. In

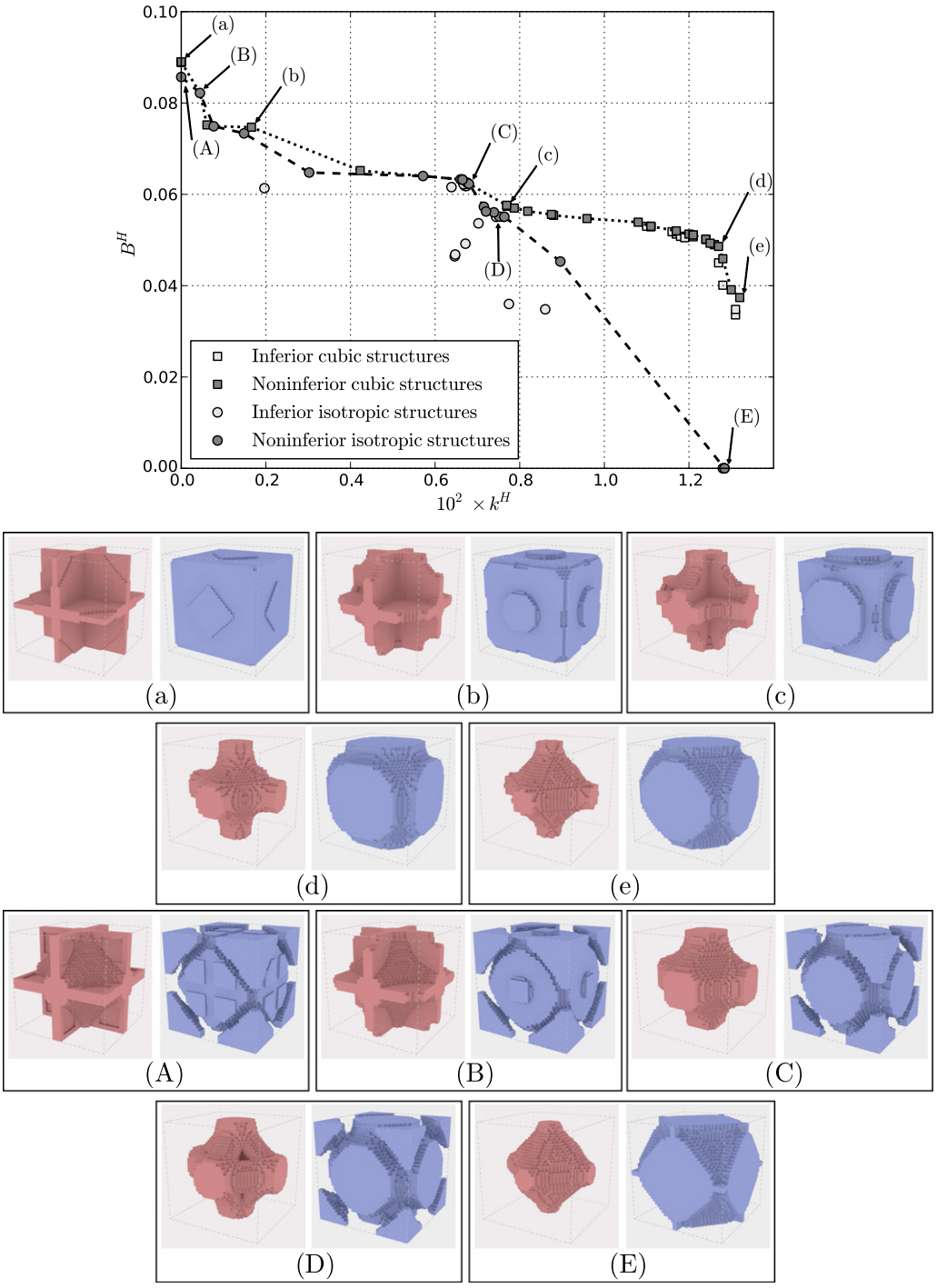

Fig. 3. Optimization results for porosity $\phi = 0.75$ with isotropic flow symmetry and both cubic (lowercase letters, star markers and dashed line) and isotropic (uppercase letters, triangular markers and solid line) elastic symmetry. The optimized base cells (a)–(E) are visualized as in Fig. 2.

Fig. 7(a), a log scale is used for the permeability to provide a clear view of the optimized properties at the three different porosities. We re-emphasize that all permeability values are scaled by the face area of the base cell and the bulk modulus values are computed with a Young's modulus of 1 and a Poisson's ratio of 0.3 for the solid phase. In Fig. 7(b), the bulk modulus values are scaled by the Hashin and Shtrikman (1963) bound, B_{HS}, for the relevant porosity; and the permeability values are scaled by the permeability k^*_{cubic} of the permeability-optimized structure with cubic elastic symmetry and isotropic flow symmetry at the same porosity. With these scalings all of the optimized results lie within the $[0,1] \times [0,1]$ square and provide a consistent picture of the upper bound of the bulk modulus and fluid permeability cross-property space.

As noted in Section 3, all the structures optimized for isotropic elastic symmetry also have perfect cubic elastic symmetry, and all of the results we have presented have perfect isotropic flow symmetry. Therefore the optimization results with isotropic elastic symmetry are naturally included in the calculation of the Pareto fronts for the cubic elastic symmetry case. This inclusion makes very little difference because the cubic optimization results generally have either equivalent or better properties than those with isotropic elastic symmetry.

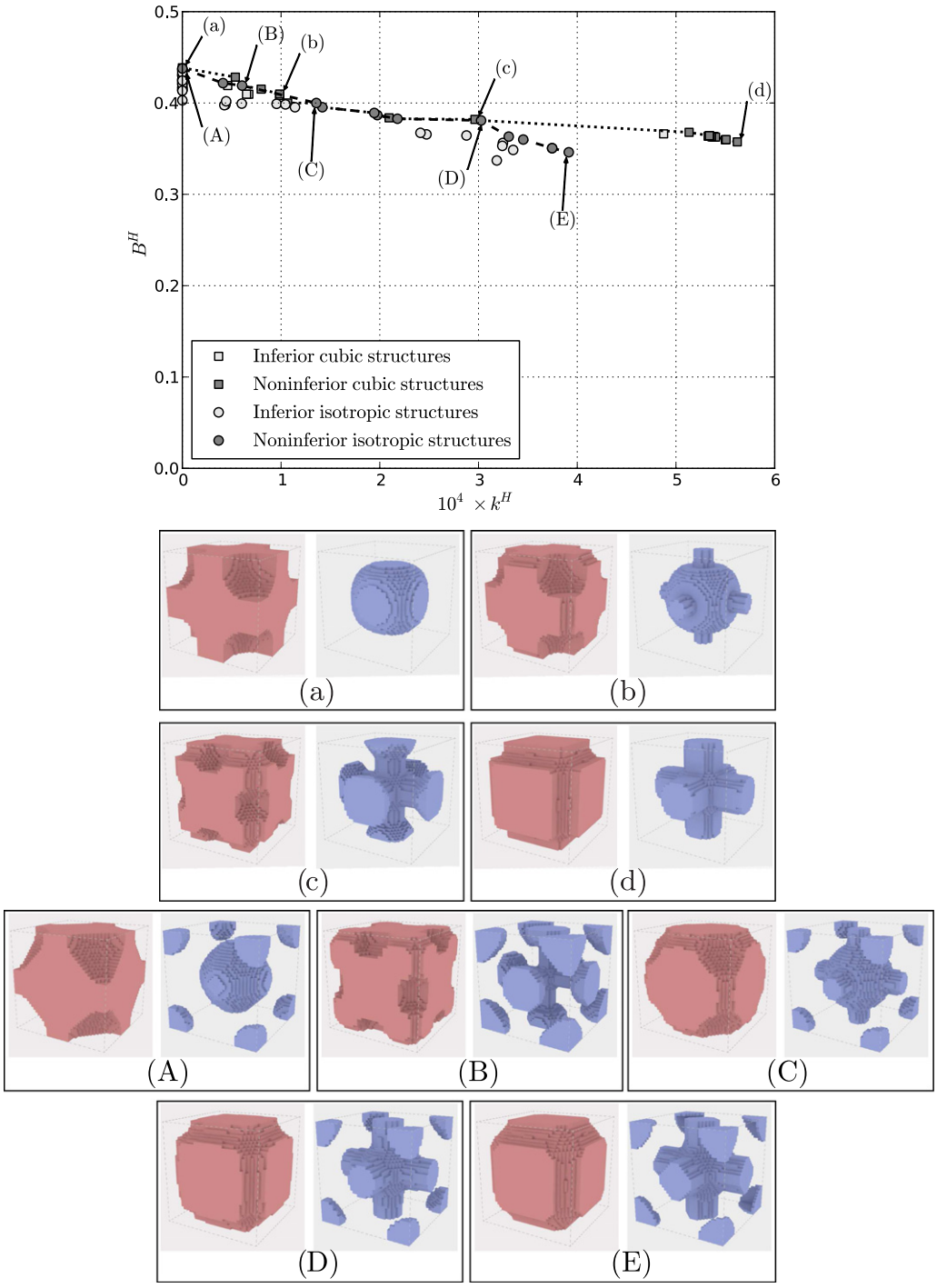

Fig. 4. Optimization results for porosity $\phi = 0.25$ with isotropic flow symmetry and both cubic (lowercase letters, star markers and dashed line) and isotropic (uppercase letters, triangular markers and solid line) elastic symmetry. The optimized base cells (a)–(E) are visualized as in Fig. 2.

Fig. 7 clearly suggests that the bulk modulus and fluid permeability cross-property space is not convex. It is therefore not surprising that the linear combination strategy (in Eq. (8)) was largely unsuccessful for finding optimization results along the interior of the Pareto fronts. This failure of the linear combination strategy contrasts with other multi-objective topology optimization work (Chen et al., 2010; de Kruijf et al., 2007; Challis et al., 2008) where the solution space is convex. This may also explain the difficulty of Guest and Prévost (2006a) in identifying topologies with high stiffness and low permeability when using a linear combination of properties. This was originally attributed to the difficulty of identifying compatible parametrizations of the continuous interpolation methods, but it now seems the non-convexity of the cross-property space may have played a significant role.

5.1. Comparison between results with cubic versus isotropic elastic symmetry

A consistent trend among the optimized topologies is that, for a given porosity, the cubic elastic solutions utilize a lattice-like organization of the void features, while the isotropic elastic solutions have a more intricate topology including smaller voids organized

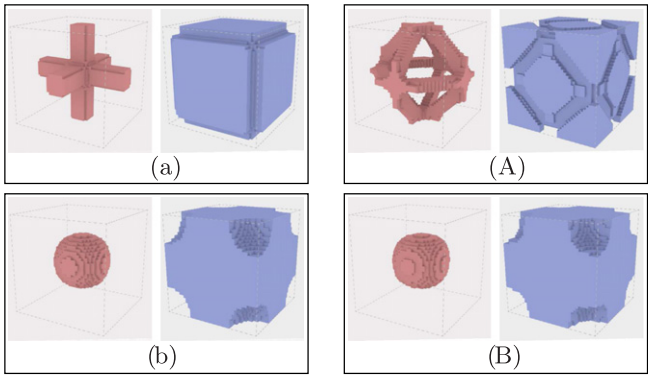

Fig. 5. Optimization results for porosity $\phi = 0.9$ with isotropic flow symmetry and either cubic elastic symmetry (a, b) or isotropic elastic symmetry (A, B). The results (a, A) arise from maximizing the bulk modulus, while (b, B) arise from maximizing the fluid permeability. The optimized base cells (a)–(B) are visualized as in Fig. 2.

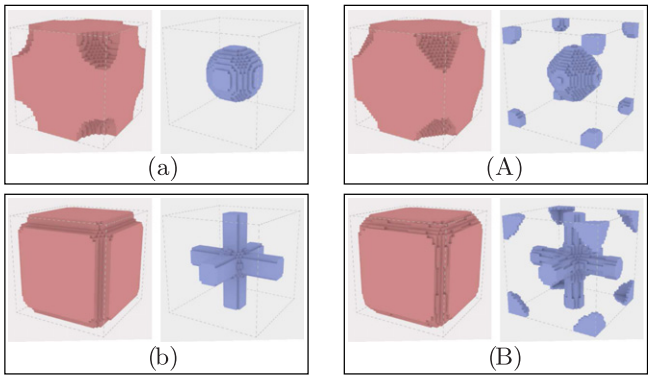

Fig. 6. Optimization results for porosity $\phi = 0.1$ with isotropic flow symmetry and either cubic elastic symmetry (a, b) or isotropic elastic symmetry (A, B). The results (a, A) arise from maximizing the bulk modulus, while (b, B) arise from maximizing the fluid permeability. The optimized base cells (a)–(B) are visualized as in Fig. 2.

Table 1
Optimization results for porosity $\phi = 0.5$, as depicted in Fig. 2.

Case	B^H	$10^3 \times k^H$	ϕ	$\mathcal{A}$
HS bound	0.2299	–	0.5	–
(a)	0.2244	0	0.4998	–
(b)	0.1840	0.72	0.5018	–
(c)	0.1703	1.85	0.4999	–
(d)	0.1579	3.10	0.5001	–
(e)	0.1473	3.42	0.5033	–
(A)	0.2253	0	0.4989	0.002
(B)	0.2101	0.18	0.5001	0.004
(C)	0.1813	1.32	0.5011	0.005
(D)	0.1731	1.98	0.4998	0.005
(E)	0.1414	2.52	0.5003	0.002
(F)	0	2.86	0.5006	0

in a more staggered pattern. This is clearly seen, for example, in the maximum bulk modulus solutions of Fig. 2(a) and (A) where the void phase of the cubic solution consists of a single body in the center of the base cell, whereas the isotropic solution features one void body at the center of the base cell and another at the corner. We highlight the interesting topologies in Fig. 2(B) and (C) that have two disconnected sets of channels through which fluid can flow. Most of the other elastically isotropic topologies have a disconnected portion of void phase where fluid would not flow: such portions do not contribute to the fluid permeability but are needed to result in a porous material that is elastically isotropic.

Fig. 7 clearly shows that in the low permeability regime the two different elastic symmetry requirements result in similar high bulk modulus regions of the Pareto fronts, despite the disconnected void regions in the elastically isotropic solutions. However, at the high permeability end of the Pareto fronts, this strategy of fragmenting the flow channels to achieve elastic isotropy leads to significantly inferior properties compared to the cubic elastic structures. This is due to the presence of the no-slip condition, as fluid velocities in the base cell are highly dependent on the length scales of the flow channels, and not just the total area of the flow channels. This is in contrast to properties such as conductivity, which give no significant loss in conductive performance under elastic isotropy. The effect is more pronounced at lower porosities. At $\phi = 0.25$ there is a 30% reduction in the maximum achievable fluid permeability when isotropic elastic symmetry is required. At $\phi = 0.5$ the reduction is 16%, and at $\phi = 0.75$ the reduction is only 3%. These elastically isotropic microstructures with maximized permeability also have a lower bulk modulus than their counterparts with cubic elastic symmetry. In fact, at $\phi = 0.5$ and $\phi = 0.75$, these isotropic microstructures have a disconnected solid phase so have zero stiffness (Figs. 2(F) and 3(E)) – the optimization algorithm has disconnected the solid phase to ensure an isotropic elastic response of the porous material, albeit a trivial one.

5.2. Comparison of our results with earlier work

At all porosities except $\phi = 0.9$ our maximum bulk modulus solutions are Vigdergauz (1989) microstructures that are very close to attaining the upper Hashin and Shtrikman (1963) bound. For the cases with a porosity of 50% or less, the bulk modulus maximized microstructures with both cubic and isotropic elastic symmetries have bulk modulus values at least 97% of the Hashin–Shtrikman bound. At the higher porosity of $\phi = 0.75$ the bulk modulus maximized microstructures attain at least 91% of the Hashin–Shtrikman bound. This is confirmed in Fig. 7. The case of $\phi = 0.9$ is discussed below in Section 5.3.

Where our results can be directly compared to material design results presented previously they are consistent with that earlier work. This includes the bulk modulus maximized structures for both the cubic and isotropic elastic symmetry cases at all porosities except $\phi = 0.9$ (Sigmund, 1999, 2000; Guest and Prévost, 2006a; Challis et al., 2008), and the maximum permeability structure with cubic elastic symmetry for $\phi = 0.5$ (Fig. 2(e)) (Guest and Prévost, 2007). The value of the permeability for the structure presented in Fig. 2(e) is slightly higher in our work, likely due to the use of $40 \times 40 \times 40$ finite elements in the base cell rather than $30 \times 30 \times 30$ used by Guest and Prévost (2007). Our value is also comparable to that reported by Jung and Torquato (2005) for the Schwartz primitive topology.

In addition, we can compare the $\phi = 0.5$ results for the cubic elastic symmetry case (Fig. 2(a)–(e)) to those presented by Guest and Prévost (2006a). The geometry of the unit cell looks somewhat different in structures (b) and (c), however the overall topology of all of the designs is consistent with this earlier work. The actual bulk modulus and permeability properties of the structures cannot be compared directly because Guest and Prévost (2006a) used a Poisson's ratio of 0.33 instead of the value of 0.3 used here. A combined permeability and stiffness objective function has also been considered by Chen et al. (2011) for the purpose of tissue engineering. Our optimized material microstructures presented in Fig. 2(a)–(c) are similar to the high stiffness microstructures presented by Chen et al. (2011). The disparity between the other microstructures presented is not surprising given the major differences between the objective formulations in the two pieces of work.

We can also compare our results with earlier work maximizing the bulk modulus and conductivity with a requirement of isotropy

Table 2
Optimization results for porosity $\phi = 0.75$, as depicted in Fig. 3.

Case	B^H	$10^2 \times k^H$	ϕ	$\mathcal{A}$
HS bound	0.0939	-	0.75	–
(a)	0.0890	0	0.7495	–
(b)	0.0747	0.17	0.7513	–
(c)	0.0574	0.77	0.7503	–
(d)	0.0486	1.27	0.7524	–
(e)	0.0374	1.32	0.75	–
(A)	0.0857	0	0.7498	0.001
(B)	0.0822	0.04	0.75	0.001
(C)	0.0623	0.68	0.75	0.0008
(D)	0.0551	0.76	0.7499	0.0007
(E)	0	1.28	0.7506	0

Table 3
Optimization results for porosity $\phi = 0.25$, as depicted in Fig. 4.

Case	B^H	$10^4 \times k^H$	ϕ	$\mathcal{A}$
HS bound	0.4444	–	0.25	–
(a)	0.4385	0	0.2521	–
(b)	0.4098	1.0	0.2479	–
(c)	0.3820	3.0	0.2433	–
(d)	0.3574	5.6	0.2548	–
(A)	0.4378	0	0.2489	0.0005
(B)	0.4190	0.6	0.2503	0.0004
(C)	0.4000	1.4	0.2506	0.002
(D)	0.3809	3.0	0.2504	0.001
(E)	0.3461	3.9	0.2503	0.001

Table 4
Optimization results for porosity $\phi = 0.9$, as depicted in Fig. 5.

Case	B^H	$10^2 \times k^H$	ϕ	$\mathcal{A}$
HS bound	0.0338	–	0.9	–
(a)	0.0157	2.67	0.9001	–
(b)	0	4.89	0.9009	–
(A)	0.0165	0.87	0.8999	0.003
(B)	0	4.75	0.9009	0

Table 5
Optimization results for porosity $\phi = 0.1$, as depicted in Fig. 6.

Case	B^H	$10^5 \times k^H$	ϕ	$\mathcal{A}$
HS bound	0.6452	-	0.1	–
(a)	0.6418	0	0.1003	–
(b)	0.5912	6.8	0.1003	–
(A)	0.6389	0	0.1003	0.0003
(B)	0.5784	4.0	0.1003	0.0005

(Challis et al., 2008). The permeability and bulk modulus of the isotropic structures from Fig. 6 and Table 3 of Challis et al. (2008) are plotted with star markers in Fig. 2. It is clear that bulk modulus and permeability properties of the structures from Challis et al. (2008) are inferior to the properties of the structures presented here. One major difference that arises from using the permeability objective instead of the conductivity objective is that the convexity of the bulk modulus and conductivity cross-property space (Gibiansky and Torquato, 1996) means that structures on the Pareto front can readily be found by maximizing a linear combination of the bulk modulus and conductivity. In addition, unlike maximizing the conductivity, which must disconnect the stiff phase of the microstructure, maximizing the permeability does not disconnect the stiff phase in many cases. Finally, in the work of Challis et al. (2008) the stiff and conductive phases were typically both connected for isotropic multifunctional microstructures with intermediate properties, and this meant that scaffolds of the stiff phase were able to be fabricated by solid freeform fabrication (Challis et al., 2010). In the permeability case the intricacy of the isotropic designs presented here may not allow them to be manufactured by solid freeform fabrication. These differences have important implications regarding the design and manufacture of bone implant scaffolds (Hollister, 2005, 2009; Challis et al., 2010).

5.3. Limitations

A limitation of the current work is that design freedom is significantly restricted at low and high porosities. This is because the optimization method struggles to resolve the optimal microstructures with $40 \times 40 \times 40$ elements in the base cell. We have therefore not attempted to identify enough meaningful data points to generate Pareto fronts at the porosities of $\phi = 0.1$ and $\phi = 0.9$. Despite these limitations, we are confident that the

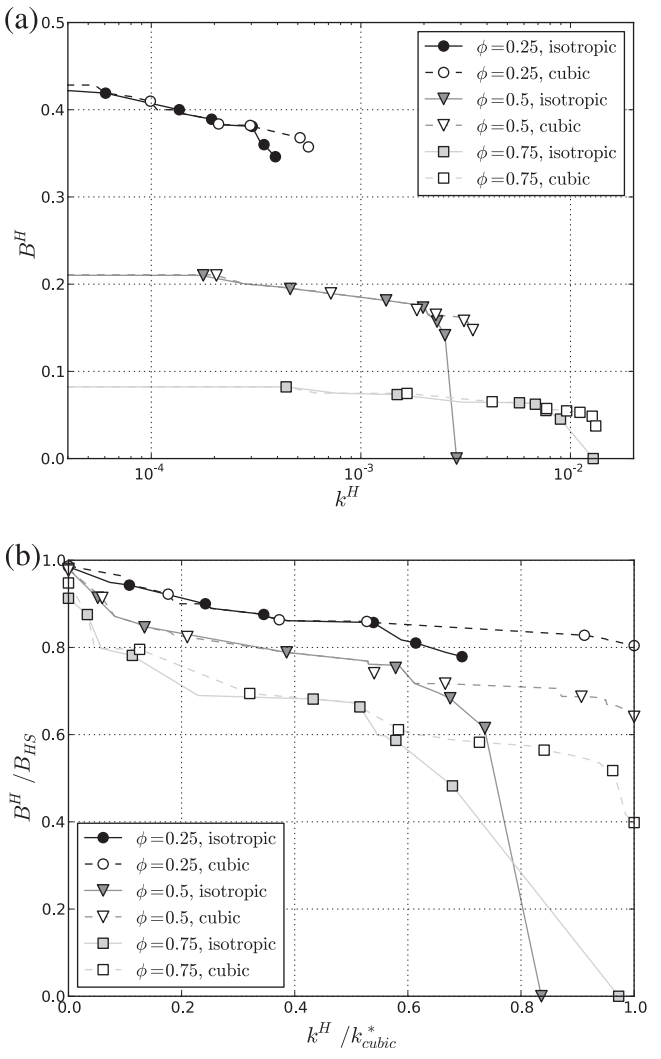

Fig. 7. Two views of the Pareto fronts for porosities $\phi = 0.25$, $\phi = 0.5$ and $\phi = 0.75$ together on the same axes, with the properties of selected structures marked. In (a), a log scale is utilized for the permeability. In (b), the properties for each porosity are scaled to fit within the $[0, 1] \times [0, 1]$ square, as described in the text. All optimization results have isotropic flow symmetry as well as the elastic symmetry indicated in the legend.

Table 6
The properties of bi-optimal porous materials.

ϕ	B^H	k^H	Base cell
Cubic elastic and isotropic flow symmetry			
0.10	0.5912	6.8×10^{-5}	Fig. 6(b)
0.25	0.3574	5.6×10^{-4}	Fig. 4(d)
0.50	0.1473	3.42×10^{-3}	Fig. 2(e)
0.75	0.0486	1.27×10^{-2}	Fig. 3(d)
0.90	0.0157	2.67×10^{-2}	Fig. 5(a)
Isotropic elastic and isotropic flow symmetry			
0.10	0.5784	4.0×10^{-5}	Fig. 6(B)
0.25	0.3461	3.9×10^{-4}	Fig. 4(E)
0.50	0.1414	2.52×10^{-3}	Fig. 2(E)
0.75	0.0623	6.8×10^{-3}	Fig. 3(C)
0.90	0.0165	8.7×10^{-3}	Fig. 5(A)

permeability-maximized results for $\phi = 0.9$ presented in Fig. 5(b) and (B) and the results for $\phi = 0.1$ in Fig. 6 are representative of the optimal microstructures. In particular, the bulk modulus maximized results for $\phi = 0.1$ are very close to attaining the Hashin–Shtrikman bound (as noted above in Section 5.2).

The difficulty of attaining optimal microstructures at high porosity is apparent in the maximized bulk modulus microstructures with $\phi = 0.9$ (Fig. 5(a) and (A)). These results are clearly not optimal: they do not reflect the known optimal Vigdergauz (1989) microstructures and are significantly below the Hashin–Shtrikman bound. It is clear that this discrepancy is due to a failure to resolve the maximal bulk modulus structures for $\phi = 0.9$ with $40 \times 40 \times 40$ finite elements. For the cubic elastic symmetry case, one can calculate that approximately 15% of these 64,000 elements need to be solid to generate three axis-aligned planes that disconnect the void phase (as in Fig. 3(a), for example), and this is larger than the 10% of elements allowed to be solid for $\phi = 0.9$. However, we also note that the microstructures presented in Fig. 5(a) and (A) may belong on the Pareto front, even though they are not the maximum bulk modulus microstructures.

The presented Pareto fronts were obtained using the three-dimensional cross structure as the initial condition. To determine if this restricted the bounds determined for the cross-property space, we performed additional optimizations with initial unit cells derived from the Schwartz diamond and the Schoen gyroid surfaces. These optimizations resulted in porous materials with significantly inferior properties to those presented here. We expect this is because a simple topology with large pore channels is advantageous for maximizing the fluid permeability. For the same reason, we do not expect microstructures with more than one length scale to be optimal for the bulk modulus and permeability problem.

Further, we also note that the cubic symmetry of the starting cross structure is naturally maintained during the optimization process. This means that microstructures that are elastically cubic or isotropic but which do not have explicit cubic symmetry of the base cell are not found with our optimization algorithm. However, we do not believe this significantly restricts the Pareto fronts we have presented. Indeed, for the related problem of jointly optimizing bulk modulus and conductivity considered in Challis et al. (2008), a similar situation occurred. For that problem, theoretical cross-property bounds are available, and the (symmetric) topology optimized structures attained properties very close to these bounds.

5.4. Bi-optimal porous materials

Although the Pareto fronts provide a comprehensive solution to the optimization problem, it is also useful to highlight the microstructures at each porosity that have excellent multifunctional properties. We have found such bi-optimal structures from the computationally-derived Pareto fronts by determining which of the noninferior solutions on each front maximizes the objective

$$f(B^H(\boldsymbol{\rho}), k^H(\boldsymbol{\rho})) = \frac{1}{2}\left[\frac{B^H(\boldsymbol{\rho})}{B^*} + \frac{k^H(\boldsymbol{\rho})}{k^*}\right]. \tag{10}$$

This is the optimization objective in Eq. (8) with $\omega_B = \frac{1}{2}$ and $\omega_k = \frac{1}{2}$. The properties of these bi-optimal materials are listed in Table 6 and are shown graphically in Fig. 8.

Fig. 8 demonstrates the trade-off between the bulk modulus and fluid permeability achievable with a multifunctional porous material over a range of porosities, including the $\phi = 0.1$ and

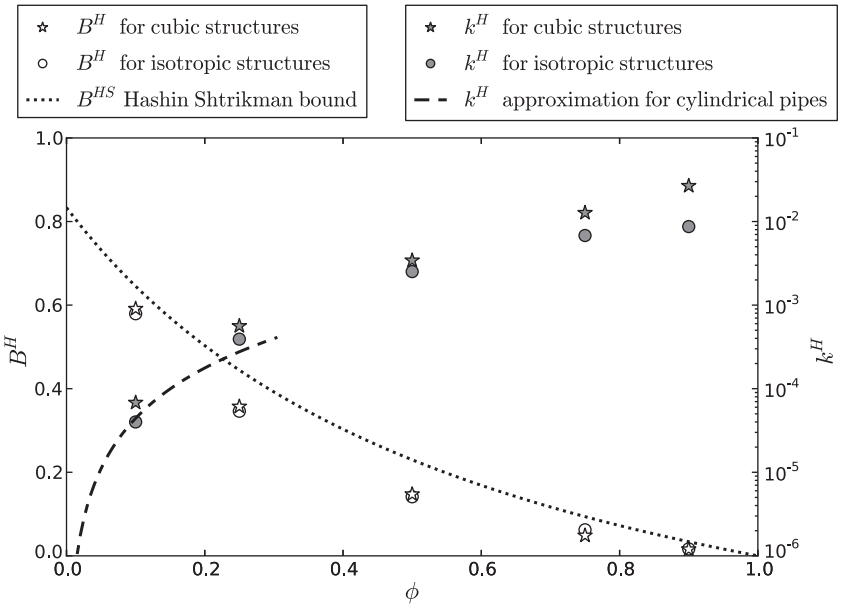

Fig. 8. The properties of porous materials that are bi-optimal for bulk modulus and fluid permeability. Also shown are the upper Hashin–Shtrikman bound for the bulk modulus (dotted line) and the fluid permeability for three axis-aligned, non-intersecting circular cylinders of void phase (dashed line, Torquato, 2002). All optimization results have isotropic flow symmetry as well as the elastic symmetry indicated in the legend.

$\phi = 0.9$ results. It is clear that the elastically isotropic structures in general have slightly inferior multifunctional properties compared to those achievable with the requirement of cubic elastic symmetry. Further, for low and medium porosities a high permeability is achieved with a fairly minor reduction of the bulk modulus below the Hashin–Shtrikman bound.

We suggest these bi-optimal porous materials to practitioners wanting multifunctional porous materials that have good properties for both the bulk modulus and the fluid permeability. We note that these bi-optimal designs are robust: although they are only optimal for the case of equal weighting in the objective function, they will still perform well for a range of weights in Eq. (8).

6. Conclusion

We have presented Pareto fronts that estimate the upper bound of the bulk modulus and fluid permeability cross-property space for periodic porous materials with porosities of 0.25, 0.5 and 0.75. We have considered the two cases of: (1) isotropic flow symmetry with cubic elastic symmetry; and (2) isotropic flow symmetry with isotropic elastic symmetry. Many new topology optimized base cells are presented for both cases. The isotropic elastic symmetry requirement results in more intricate topologies than the cubic elastic symmetry case. The fluid permeability is influenced both by the total void channel area and the length scales of the void channels, and hence the intricacy of the elastically isotropic topologies results in a decrease in the extent of the bulk modulus and fluid permeability cross-property space compared to the case of cubic elastic symmetry. This is in contrast with other properties that are length-scale independent (such as the bulk modulus and conductivity cross-property bounds), and occurs due to the no-slip condition of the fluid at the solid–fluid interface.

This work should be useful for designing materials for which stiffness and permeability are desired properties, especially given the lack of microstructure-independent theoretical cross-property bounds. Our computational estimates of the range of achievable properties for various porosities will aid in both material phase selection and in the assessment of designed structures.

Acknowledgments

This research was supported by the Australian Research Council's Discovery Projects DP0878785 and DP110101653. This financial support is gratefully acknowledged. Author JK Guest also acknowledges support by the Defense Advanced Research Projects Agency (DARPA) under the Materials with Controlled Microstructural Architectural (MCMA) Program. Computational resources used in this work were provided by the Queensland Cyber Infrastructure Foundation.

Appendix A. Shape derivative for the fluid permeability

Fluid flow through a porous material is governed by Darcy's law on the macroscopic scale. In indicial notation with the summation convention assumed, Darcy's law is given by

$$U_i = -\frac{1}{\mu} K^H_{ij} P_j, \tag{A.1}$$

where U_i is the average fluid velocity vector, μ is the viscosity, $K^H_{ij} (\equiv \boldsymbol{K}^H)$ is the fluid permeability tensor, and P_i is the pressure gradient (Sanchez-Palencia, 1980; Torquato, 2002). The fluid permeability tensor is calculated via homogenization: K^H_{ij} is an ensemble average of fluid velocities in the base cell given by

$$K^H_{ij} = \langle w_{ij} \rangle, \tag{A.2}$$

where $\langle \cdot \rangle$ is the ensemble average and w_{ij} satisfies the scaled Stokes equations (Torquato, 2002)

$$w_{ji,kk} - \Pi_{i,j} = -\delta_{ji} \quad \text{in } \Omega, \tag{A.3}$$

$$w_{ji,j} = 0 \quad \text{in } \Omega, \tag{A.4}$$

$$w_{ji} = 0 \quad \text{on } \partial\Omega. \tag{A.5}$$

Here Π_i is the characteristic pressure field, Ω is the domain occupied by the fluid and δ_{ij} is the Kronecker delta. The homogenized permeability tensor in an ergodic medium can be usefully re-written as

$$K^H_{ij} = \langle w_{ki,l} w_{kj,l} \rangle, \tag{A.6}$$

where the ensemble average can be replaced by the volume average

$$\langle \phi \rangle = \frac{1}{|Y|} \int_Y \phi, \tag{A.7}$$

with Y representing the base unit cell (Guest and Prévost, 2007).

We present the following Lagrangian (Allaire et al., 2004; Céa, 1986) that is suitable for calculating the shape derivative of each component K^H_{ij} of the fluid permeability tensor for both the $i = j$ and $i \neq j$ cases:

$$L_{ij} = \frac{1}{|Y|} \left(- \int_\Omega w_{ki,l} w_{kj,l} - \int_\Omega w_{ki} \Pi_{j,k} - \int_\Omega w_{kj} \Pi_{i,k} + \int_\Omega w_{ki} \delta_{kj} + \int_\Omega w_{kj} \delta_{ki} + \int_{\partial\Omega} w_{ki} n_l w_{kj,l} + \int_{\partial\Omega} w_{kj} n_l w_{ki,l} \right). \tag{A.8}$$

The Lagrangian generates the correct equations of motion (Eqs. (A.3)–(A.5)) for the velocities w_{ij} and reduces to the components of the homogenized permeability tensor K^H_{ij} when these equations of motion are satisfied. Taking the shape derivative of the Lagrangian and evaluating at the equations of motion gives the shape derivative of the components of the fluid permeability tensor as

$$\frac{\mathrm{d}K^H_{ij}}{\mathrm{d}\Omega}(\theta) = \frac{1}{|Y|} \int_{\partial\Omega} \theta_m n_m w_{ki,l} w_{kj,l}. \tag{A.9}$$

The three shape derivatives of the components K^H_{11}, K^H_{22} and K^H_{33} are easily combined to give the shape derivative of the scalar fluid permeability k^H for the isotropic flow case using the relation

$$k^H = \frac{1}{3} (K^H_{11} + K^H_{22} + K^H_{33}). \tag{A.10}$$

For a similar shape derivative calculation presented with more detailed explanations, the reader is referred to the derivation of the shape derivative of the energy dissipation objective function for Stokes flows by Challis and Guest (2009).

References

Allaire, G., Jouve, F., Toader, A.-M., 2004. Structural optimization using sensitivity analysis and a level-set method. J. Comput. Phys. 194, 363–393.
Andreasen, C., Sigmund, O., 2011. Saturated poroelastic actuators generated by topology optimization. Struct. Multidisc. Optim. 43 (5), 693–706.
Avellaneda, M., Cherkaev, A.V., Lurie, K.A., Milton, G., 1988. On the effective conductivity of polycrystals and a three-dimensional phase-interchange inequality. J. Appl. Phys. 63, 4989–5003.
Avellaneda, M., Torquato, S., 1991. Rigorous link between fluid permeability, electrical conductivity, and relaxation times for transport in porous media. Phys. Fluids A 3 (11), 2529–2540.
Bendsøe, M.P., Sigmund, O., 2004. Topology Optimization: Theory, Methods and Applications, second ed. Springer, Berlin.
Bensoussan, A., Lions, J., Papanicolaou, G., 1978. Asymptotic Analysis for Periodic Structures. North-Holland, Amsterdam.
Bergman, D.J., 1978. The dielectric constant of a composite material a problem in classical physics. Phys. Rep. C 43, 377–407.
Berryman, J., Milton, G., 1988. Microgeometry of random composites and porous media. J. Phys. D: Appl. Phys. 21, 87–94.
Borrvall, T., Petersson, J., 2003. Topology optimization of fluids in Stokes flow. Int. J. Numer. Meth. Fluids 41, 77–107.

Céa, J., 1986. Conception optimale ou identification de formes, calcul raide de la dérivée directionnelle de la fonction coût. Math. Model. Numer. Anal. 20, 371–402 (in French).
Challis, V.J., Guest, J.K., 2009. Level-set topology optimization of fluids in Stokes flow. Int. J. Numer. Meth. Eng. 79 (10), 1284–1308.
Challis, V.J., Roberts, A.P., Grotowski, J.F., Zhang, L.C., Sercombe, T.B., 2010. Prototypes for bone implant scaffolds designed via topology optimization and manufactured by solid freeform fabrication. Adv. Eng. Mater. 12 (11), 1106–1110.
Challis, V.J., Roberts, A.P., Wilkins, A.H., 2008. Design of three dimensional isotropic microstructures for maximized stiffness and conductivity. Int. J. Solids Struct. 45, 4130–4146.
Chen, Y., Zhou, S., Li, Q., 2009. Computational design for multifunctional microstructural composites. Int. J. Mod. Phys. B 23, 1345–1351.
Chen, Y., Zhou, S., Li, Q., 2010. Multiobjective topology optimization for finite periodic structures. Comput. Struct. 88, 806–811.
Chen, Y., Zhou, S., Li, Q., 2011. Microstructure design of biodegradable scaffold and its effect on tissue regeneration. Biomaterials 32, 5003–5014.
Cherkaev, A.V., Gibiansky, L.V., 1993. Coupled estimates for the bulk and shear moduli of a two-dimensional isotropic elastic composite. J. Mech. Phys. Solids 41, 937–980.
Cohon, J.L., 1978. Multiobjective programming and planning. Mathematics in Science and Engineering, vol. 140. Academic Press.
de Kruijf, N., Zhou, S., Li, Q., Mai, Y.-W., 2007. Topological design of structures and composite materials with multiobjectives. Int. J. Solids Struct. 44, 7092–7109.
Garboczi, E.J., Day, A.R., 1995. An algorithm for computing the effective linear elastic properties of heterogeneous materials: three-dimensional results for composites with equal phase Poisson ratios. J. Mech. Phys. Solids 43, 1349–1362.
Gibiansky, L.V., Sigmund, O., 2000. Multiphase composites with extremal bulk modulus. J. Mech. Phys. Solids 48, 461–498.
Gibiansky, L.V., Torquato, S., 1993. Link between the conductivity and elastic moduli of composite materials. Phys. Rev. Lett. 71 (18), 2927–2930.
Gibiansky, L.V., Torquato, S., 1995. Rigorous link between the conductivity and elastic moduli of fibre-reinforced composite materials. Phil. Trans. R. Soc. Lond. A 353, 243–278.
Gibiansky, L.V., Torquato, S., 1996. Connection between the conductivity and bulk modulus of isotropic composite materials. Proc. R. Soc. Lond. A 452, 253–283.
Gibiansky, L.V., Torquato, S., 1997. Thermal expansion of isotropic multiphase composites and polycrystals. J. Mech. Phys. Solids 45 (7), 1223–1252.
Guedes, J., Kikuchi, N., 1990. Preprocessing and postprocessing for materials based on the homogenization method with adaptive finite element methods. Comput. Meth. Appl. Mech. Eng. 83, 143–198.
Guest, J.K., Prévost, J.H., 2006a. Optimizing multifunctional materials: design of microstructures for maximized stiffness and fluid permeability. Int. J. Solids Struct. 43, 7028–7047.
Guest, J.K., Prévost, J.H., 2006b. Topology optimization of creeping fluid flows using a Darcy–Stokes finite element. Int. J. Numer. Meth. Eng. 66, 461–484.
Guest, J.K., Prévost, J.H., 2007. Design of maximum permeability material structures. Comput. Meth. Appl. Mech. Eng. 196, 1006–1017.
Hashin, Z., Shtrikman, S., 1962. A variational approach to the theory of the effective magnetic permeability of multiphase materials. J. Appl. Phys. 35, 3125–3131.
Hashin, Z., Shtrikman, S., 1963. A variational approach to the theory of the elastic behaviour of multiphase materials. J. Mech. Phys. Solids 11, 127–140.
Hassani, B., Hinton, E., 1998. A review of homogenization and topology optimization II – Analytical and numerical solution of homogenization equations. Comput. Struct. 69, 719–738.
Hollister, S.J., 2005. Porous scaffold design for tissue engineering. Nat. Mater. 4, 518–524.
Hollister, S.J., 2009. Scaffold design and manufacturing: from concept to clinic. Adv. Eng. Mater. 21, 3330–3342.
Jung, Y., Torquato, S., 2005. Fluid permeabilities of triply periodic minimal surfaces. Phys. Rev. E 72 (8), 056319.
Kim, I., de Weck, O., 2005. Adaptive weighted-sum method for bi-objective optimization: Pareto front generation. Struct. Multidisc. Optim. 29, 149–158.
Kreissl, S., Pingen, G., Maute, K., 2011. An explicit level set approach for generalized shape optimization of fluids with the lattice Boltzmann method. Int. J. Numer. Meth. Fluids 65, 496–519.
Rosen, B.W., Hashin, Z., 1970. Effective thermal expansion and specific heat of composite materials. Int. J. Eng. Sci. 8, 157–173.
Sanchez-Palencia, E., 1980. Non-homogeneous Media and Vibration Theory. Lecture Notes in Physics, vol. 127. Springer, Berlin.
Schapery, R.A., 1968. Thermal expansion coefficients of composite materials based on energy principles. J. Compos. Mater. 2, 380–404.
Sevostianov, I., Kachanov, M., 2009. Connections between elastic and conductive properties of heterogeneous materials. In: Aref, H., van der Giessen, E. (Eds.), Advances in Applied Mechanics, vol. 42. Academic Press, pp. 69–252.
Sigmund, O., 1994. Materials with prescribed constitutive parameters: an inverse homogenization problem. Int. J. Solids Struct. 31 (17), 2313–2329.
Sigmund, O., 1999. On the optimality of bone microstructure. In: Bendsøe, M.P., Pedersen, P. (Eds.), IUTAM Symposium on Synthesis in Bio Solid Mechanics. Kluwer Academic Publishers., pp. 221–234.
Sigmund, O., 2000. A new class of extremal composites. J. Mech. Phys. Solids 48, 397–428.
Sigmund, O., Torquato, S., 1997. Design of materials with extreme thermal expansion using a three-phase topology optimization method. J. Mech. Phys. Solids 45 (6), 1037–1067.
Torquato, S., 2002. Random Heterogeneous Materials: Microstructure and Macroscopic Properties. Springer, New York.
Torquato, S., Hyun, S., Donev, A., 2002. Multifunctional composites: optimizing microstructures for simultaneous transport of heat and electricity. Phys. Rev. Lett. 89, 266601-1–266601-4.
Torquato, S., Hyun, S., Donev, A., 2003. Optimal design of manufacturable three-dimensional composites with multifunctional characteristics. J. Appl. Phys. 94, 5748–5755.
Vigdergauz, S., 1989. Regular structures with extremal elastic properties. Mech. Solids 24 (3), 57–63.
Walpole, L.J., 1966. On bounds for the overall elastic moduli of inhomogeneous systems I. J. Mech. Phys. Solids 14, 151–162.
Wang, M.Y., Wang, X., Guo, D., 2003. A level set method for structural topology optimization. Comput. Meth. Appl. Mech. Eng. 192, 227–246.